TU Delft

Delft University of Technology

Enhancing evapotranspiration estimates in composite terrain through the integration of satellite remote sensing and eddy covariance measurements

Ghorbanpour, Ali Karbalaye; Peddinti, Srinivasa Rao; Hessels, Tim; Bastiaanssen, Wim; Kisekka, Isaya

DOI
10.1016/j.scitotenv.2025.178530

Publication date
2025

Document Version
Final published version

Published in
Science of the Total Environment

Citation (APA)
Ghorbanpour, A. K., Peddinti, S. R., Hessels, T., Bastiaanssen, W., & Kisekka, I. (2025). Enhancing evapotranspiration estimates in composite terrain through the integration of satellite remote sensing and eddy covariance measurements. *Science of the Total Environment*, *963*, Article 178530. https://doi.org/10.1016/j.scitotenv.2025.178530

Important note
To cite this publication, please use the final published version (if applicable).
Please check the document version above.

Copyright
Other than for strictly personal use, it is not permitted to download, forward or distribute the text or part of it, without the consent of the author(s) and/or copyright holder(s), unless the work is under an open content license such as Creative Commons.

Takedown policy
Please contact us and provide details if you believe this document breaches copyrights.
We will remove access to the work immediately and investigate your claim.

This work is downloaded from Delft University of Technology.
For technical reasons the number of authors shown on this cover page is limited to a maximum of 10.

Science of the Total Environment 963 (2025) 178530

Contents lists available at ScienceDirect

Science of the Total Environment

journal homepage: www.elsevier.com/locate/scitotenv

Enhancing evapotranspiration estimates in composite terrain through the integration of satellite remote sensing and eddy covariance measurements

Ali Karbalaye Ghorbanpour [a], Srinivasa Rao Peddinti [b], Tim Hessels [c], Wim Bastiaanssen [c], Isaya Kisekka [a,b,*]

[a] Department of Biological and Agricultural Engineering, University of California, Davis, CA, USA
[b] Department of Land, Air, and Water Resources, University of California, Davis, CA, USA
[c] Department of Water Management, Delft University of Technology, Delft, the Netherlands

HIGHLIGHTS

- Optimized SEBAL improved ET accuracy by integrating eddy covariance with remote sensing.
- Utilized Bayesian inference to optimize key model parameters, reducing RMSE by up to 40 %.
- Global sensitivity analysis identified solar radiation and hot/cold pixels as influential factors.
- Validated SEBAL-OPT across diverse land uses, demonstrating optimized model robustness.

GRAPHICAL ABSTRACT

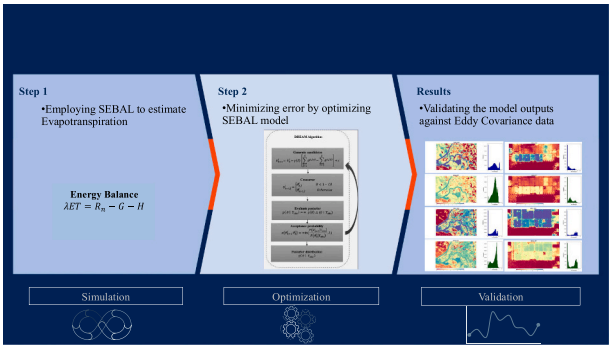

ARTICLE INFO

Editor: Christian Herrera

Keywords:
Remote sensing
Uncertainty
Eddy covariance
Energy balance
Evapotranspiration
Optimization

ABSTRACT

Accurate evaluation of water resource systems is essential for informed planning and decision-making. Evapotranspiration (ET), a key component of water resource management, is often estimated using remote sensing techniques; however, such estimates can be subject to significant uncertainties under certain conditions. In this study, we present a novel approach to improving the accuracy of ET estimates in composite terrains. The methodology involves optimizing the Surface Energy Balance Algorithm for Land (SEBAL-OPT) by integrating ground-based eddy covariance (EC) flux tower data into the satellite-based ET retrieval process. The approach was evaluated at four sites in California, each representing different land uses. Parameter optimization was achieved through Bayesian inference using the Differential Evolution Adaptive Metropolis (DREAM) algorithm, which minimized discrepancies between ET estimates derived from Landsat 8 and 9 imagery and the observed ET from EC measurements. Results from the global sensitivity analysis identified solar radiation and hot/cold pixel selection as the most sensitive parameters in the SEBAL algorithm, highlighting their critical role in reducing uncertainty in ET estimates. SEBAL-OPT demonstrated significantly improved accuracy, with root mean square error (RMSE) values ranging from 0.72 mm to 1.33 mm, compared to the original SEBAL parameterization (SEBAL-ORG), which produced RMSE values between 1.03 mm and 2.14 mm. This approach highlights that, when properly calibrated, the model can be effectively applied across diverse agricultural landscapes, regardless

* Corresponding author at: Department of Biological and Agricultural Engineering, University of California, Davis, CA, USA.
E-mail address: ikisekka@ucdavis.edu (I. Kisekka).

https://doi.org/10.1016/j.scitotenv.2025.178530
Received 14 October 2024; Received in revised form 28 December 2024; Accepted 13 January 2025
Available online 17 January 2025
0048-9697/© 2025 The Authors. Published by Elsevier B.V. This is an open access article under the CC BY license (http://creativecommons.org/licenses/by/4.0/).

of the specific land use at individual sites. These findings have significant implications for water resource planning, agricultural water management, and water rights adjudication and could be applied to other remote sensing of ET models.

1. Introduction

Agriculture accounts for a considerable portion of global water consumption (Foley et al., 2011). Accurately measuring crop water use or evapotranspiration (ET) is critical to managing water use in agriculture. The quest for sustainability in water resources management is inherently linked to ensuring food security, necessitating accurate estimations of water consumption. ET is a key concept in understanding and quantifying the dynamics of the hydrological cycle. ET encapsulates the combined processes of evaporation, and transpiration representing the amount of water released into the atmosphere from soil and plant surfaces and the quantity released via the plant stomata, respectively (Allen et al., 1998; Monteith, 1981; Penman, 1948). This important hydrologic flux signifies the water utilized by crops and serves as a fundamental indicator in assessing the water needs of agricultural systems (L. Zhang et al., 2019). Accurately estimating crop water consumption is essential for informed decision-making and effective planning. Reliable data on ET plays a critical role in enabling policymakers, agricultural stakeholders, and resource managers to make informed decisions regarding water allocation, crop selection, irrigation management strategies, and during adjudication of water rights disputes.

In hydrologic water balance modeling and irrigation management, ET is the key factor that drives water allocation and significantly influences water demand. At the local scale, various methods, such as lysimeters and eddy covariance systems (Baldocchi et al., 2001; Nagler et al., 2005; Paul et al., 2013; Peddinti and Kisekka, 2022a), have been used to estimate ET. In addition, physical-mathematical models like the Penman-Monteith method, combined with crop coefficients (Allen et al., 1998; Jensen & Wright, 1970; Karimzadeh et al., 2024) are commonly applied. However, these approaches rely on ground-based measurements, which face challenges when scaling to larger, heterogeneous landscapes (Bastiaanssen and Steduto, 2017). Additionally, routine direct measurement of ET proves laborious and logistically challenging to sustain. In contrast, optical and thermal satellite data used in surface energy balance models such as SEBAL (Bastiaanssen et al., 1998a), METRIC (Allen et al., 2007a), TSEB (Kustas and Norman, 1999), SEBS (Su, 2002), and ALEXI (Anderson et al., 2011), offer a promising alternative for ET estimation. Yet, comparative studies of remote sensing-based ET methods have not consistently identified a clear best option (Sriwongsitanon et al., 2020; Tran et al., 2023; Volk et al., 2023). Satellite-based ET models inherently involve various sources of uncertainty and error, including inaccuracies in input data, data processing, and model parameters (L. Zhang et al., 2023). These uncertainties can propagate through the modeling process, potentially affecting the final outputs (FAO, 2023). Unaddressed, these uncertainties pose challenges to effective policymaking for stakeholders reliant on such data. The past decade has witnessed the emergence of publicly accessible ET products, such as SSEBop (Senay et al., 2022), WaPOR (FAO, 2018), and OpenET (Melton et al., 2022), which have become available, emphasizing the growing need for accurate ET estimations with quantified uncertainty.

There is a notable gap in the literature regarding comprehensive uncertainty analysis for remotely sensed ET and strategies focused on minimizing errors. ET varies highly across spatial domains, and field conditions differ significantly from catchment-average ET conditions. Wolff et al. (2022) introduced an optimization framework that integrates pixel selection into the SEBAL algorithm to reduce the differences between modeled and measured ET. Pixel selection is critical in energy balance models like SEBAL and METRIC, significantly affecting model accuracy. Efforts have been made to automate this process (e.g., Bhattarai et al., 2017; Silva et al., 2019), but automation alone has not sufficiently reduced uncertainties in the final outputs. However, automating pixel selection alone has not adequately reduced uncertainty in final outputs. Long et al. (2011) examined the uncertainties introduced by changes in sensor resolution and input variables in SEBAL, emphasizing the sensitivity of heat flux estimates to anchor pixel temperatures. The subjective selection of "hot" and "cold" pixels, influenced by factors like domain size, cloud cover, soil type, and vegetation, introduces substantial uncertainties and propagates errors in SEBAL-based ET estimates (Gao et al., 2008; Marx et al., 2008; Saboori et al., 2021). On the other hand, ground-based data accuracy is subject to different challenges. Global studies on eddy covariance indicate energy balance closure errors ranging from 10 % to 20 % (Peddinti and Kisekka, 2022b). Jensen and Allen (2016) reviewed various ET measurement methods and noted that each method has inherent limitations. While some studies have explored the sensitivity of input variables and model parameters on SEBAL outputs, none have systematically conducted a global sensitivity analysis (SA) or developed a scoring system to identify key parameters that require careful consideration for accuracy (Teixeira et al., 2009; Wang et al., 2009). These limitations highlight the ongoing challenge of quantifying and mitigating uncertainties in remotely sensed ET models.

Several methodologies have been developed to quantify both parameter and model uncertainty. Techniques such as sequential uncertainty fitting (SUFI-2) (Abbaspour et al., 2007, 2015), generalized likelihood uncertainty estimation (GLUE) (Beven and Freer, 2001), Bayesian approaches including Markov Chain Monte Carlo (MCMC) (Kuczera and Parent, 1998; Shi et al., 2023; Xie et al., 2009) aim to derive posterior distributions of unknown parameters based on available information and observed data. Beyond uncertainty analysis, effective modeling also requires identifying the individual contributions of each input or parameter to overall uncertainty (Saltelli et al., 2019; Song et al., 2015). To address this, SA methods like the Sobol method (Sobol, 2001), Fourier Amplitude Sensitivity Test (McRae et al., 1982; Saltelli and Bolado, 1998), and Morris One-at-a-time (Morris, 1991; Kisekka et al., 2013) have been developed. These methods evaluate how variations in input assumptions and parameters affect model outcomes within their respective ranges. While SA explores the relationship between input variations and model outcomes, uncertainty analysis quantifies the overall uncertainty within the model, irrespective of specific input assumptions (Saltelli et al., 2019). Although ET estimates play a critical role in hydrologic studies and irrigation management, there remains a significant gap in the literature regarding comprehensive uncertainty analysis, specifically for remote sensing-based ET models. This lack of focus on quantifying and addressing uncertainties arising from varying inputs, assumptions, and model parameters hinders the reliability and confidence in ET data used for decision-making in water resource management and agricultural planning.

This study uses the SEBAL model, which estimates spatial ET based on surface energy balance principles and identifies hot and cold pixels through empirical equations. However, inherent uncertainties arise due to the model's simplifications and assumptions. The primary objective of this research is to identify and prioritize the most influential parameters within the SEBAL model through global sensitivity analysis. We aim to highlight key areas for minimizing errors in SEBAL and similar remote sensing models by ranking these parameters. Another goal of the study is to reduce discrepancies between SEBAL-derived ET and measured ET values by integrating the SEBAL algorithm with the Bayesian-based global optimization technique DREAM (DiffeRential Evolution Adaptive Metropolis) (Vrugt, 2016; Vrugt et al., 2009). DREAM, which utilizes a Markov Chain Monte Carlo (MCMC) sampling scheme, efficiently addresses parameter uncertainties and determines the posterior

distributions of model parameters. The methodology involves two approaches: first, performing a one-year calibration of SEBAL and validating it against other years (temporal validation), and second, calibrating SEBAL at a single station and validating it across different locations with varying land uses (spatial validation).

2. Materials and methods

2.1. Study area description and data collection

This study utilized ground-truth data and Landsat imagery collected from multiple locations in California's Central Valley, including a commercial almond orchard and three eddy covariance flux tower stations within the AmeriFlux network (https://ameriflux.lbl.gov/). The flux towers continuously monitor ecosystem-level carbon, water, and energy fluxes. Fig. 1 illustrates the location of the study sites, and Table 1 provides detailed site characteristics, including data collection periods, land use types, and geographic coordinates.

2.1.1. CAPEX almond orchard

The primary ground-truth data was collected from a commercial almond orchard located at California Almond Packers and Exporters (CAPEX) in the northern Sacramento Valley near Corning, California (39.95°N, −122.24°W). This site primarily consists of three almond varieties—Nonpareil-Peach, Butte-Marianna, and Monterey-Peach—each grafted onto their respective rootstocks. The orchard is characterized by tree spacings of 4.8 m and a consistent row spacing of 6.7 m. The region's climate is classified as warm Mediterranean according to the Köppen climate classification system, with an annual mean temperature of 16.6 °C and an average annual precipitation of 548 mm, the majority of which occurs during the winter months. These climatic conditions are ideal for almond production. Irrigation at this site is conducted via a micro-sprinkler system with a spacing of 6.7 m. The soil composition at the CAPEX site is heterogeneous, consisting of silt loam, silty clay loam, and loam, with notable lateral and vertical variations.

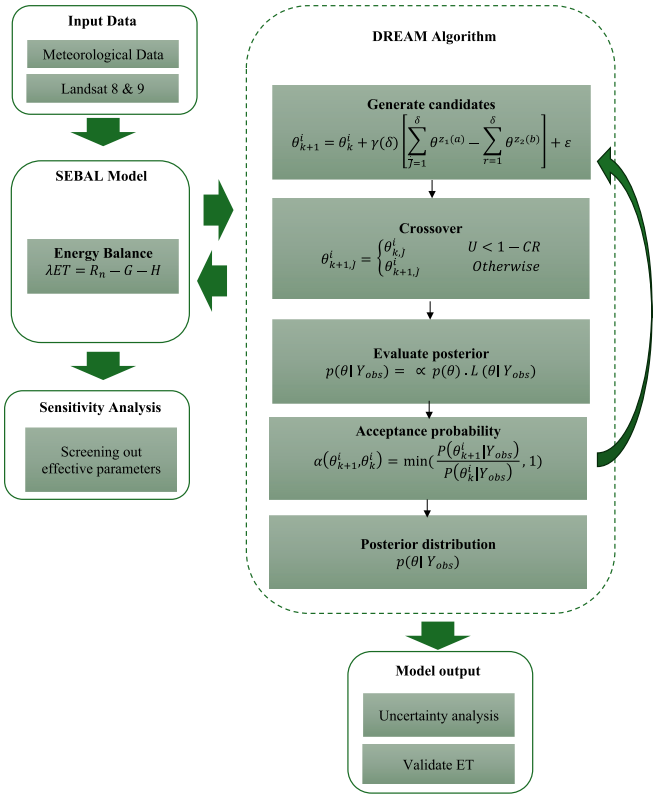

Fig. 1. Framework of the proposed optimization method.
θ^i_{k+1} and θ^i_k: Represents the candidate solution that is being generated in the k-th and (k + 1)-th generation, $\gamma(\delta)$: Scaling factor, adjusting the perturbation size, $\theta^{z_1(a)}$ and $\theta^{z_2(b)}$: Two parameter vectors chosen randomly from the current population, U: is a random number from a uniform distribution (0,1), CR: is the crossover probability, $P(\theta^i_k|Y_{obs})$: This is the posterior distribution of the current state given the observed data (Y_{obs}), $P(\theta^i_{k+1}|Y_{obs})$: This is the posterior distribution of the proposed state given the observed data, ε: Random noise.

2.1.2. AmeriFlux tower sites

In addition to the CAPEX almond orchard, this study utilized data from three AmeriFlux flux tower stations: US-Bi1, US-Bi2, and US-Myb. These sites in central California span diverse land uses—alfalfa, corn, and permanent wetland, respectively—providing a broad range of ecological and agricultural conditions for evaluating evapotranspiration (ET). The US-Bi1 site (38.1°N, −121.5°W) is primarily dedicated to alfalfa cultivation, while the US-Bi2 site (38.11°N, −121.54°W) focuses on corn production. The US-Myb site (38.05°N, −121.75°W) is in a permanent wetland ecosystem. Data were collected from all three sites over the same period, spanning from February 2018 to December 2021. All three sites were equipped with eddy covariance systems that continuously measure water, energy, and carbon fluxes. These high-resolution flux measurements serve as critical ground-truth data, providing a solid foundation for validating remotely sensed ET estimates derived from the SEBAL model. Incorporating data from these ecologically diverse sites ensures a comprehensive assessment of SEBAL's performance across varying land use types and environmental conditions.

2.1.3. Landsat imagery

Cloud-free Landsat 8 and 9 images, covering the geographical regions of CAPEX and the AmeriFlux flux tower sites, were acquired from the United States Geological Survey (USGS) via the Earth Explorer platform (http://earthexplorer.usgs.gov). The imagery from the Operational Land Imager (OLI) and the Thermal Infrared Sensor (TIRS) was collected during the designated data collection periods as outlined in Table 1. These satellite images served as the primary input for the SEBAL (Surface Energy Balance Algorithm for Land) model, providing essential spatial and spectral data for estimating ET across different land use types and climatic conditions. To enhance the accuracy of the analysis, each Landsat image underwent preprocessing tailored to the specific requirements of the study areas. This included geometric correction, atmospheric correction, and radiometric calibration to ensure the consistency and reliability of the derived ET estimates. In addition to the satellite imagery, a Digital Elevation Model (DEM) with a spatial resolution of 30 m, obtained from the Shuttle Radar Topography Mission (SRTM), was incorporated into the analysis. The DEM data helped account for variations in topography and elevation, further improving the precision of the energy balance calculations and providing a more comprehensive assessment of the SEBAL model's performance in diverse environments.

2.2. Micrometeorological data and processing

At the CAPEX site, an eddy covariance (EC) flux tower was installed to measure high-frequency turbulent fluxes, including ET. The system comprised a 3D sonic anemometer (Gill R3–50, Li-Cor, USA) for measuring wind velocity in three dimensions and an open-path gas analyzer (LI-7500, Li-Cor Inc., Lincoln, NE) mounted at a height of 10 m to measure CO2 and H2O fluxes at a frequency of 10 Hz. In addition to these measurements, various Biomet sensors were deployed to monitor environmental conditions. A four-component net radiometer (SN-500-SS, Apogee Instruments, Inc., UT, USA) measured net radiation. At the same time, three soil heat flux plates (HFT-3, Radiation Energy Balance Systems, Bellevue, WA) were inserted at a depth of 8 cm to assess soil heat flux. Complementary measurements included three soil

Table 1
Geographic coordinates, land use types, and data collection periods for CAPEX almond orchard and AmeriFlux tower sites.

Site	Number of images	Lat	Lon	Mean annual Precipitation (mm)	Mean annual temperature (C°)	Elevation (m)	Land use type	Eddy Covariance data availability
CAPEX	66	39.95	−122.24	548	16.6	89	Almond	2020/9–2022/8
US-Bi1	54	38.1	−121.5	338	16	−2.7	Alfalfa	2018/2–2021/12
US-Bi2	54	38.11	−121.54	338	16	−5	Corn	2018/2–2021/12
US-Myb	54	38.05	−121.75	338	15.9	−4	Permanent wetland	2018/2–2021/12

thermocouples (TCAV-L, Campbell Scientific Inc., Logan, UT) and soil moisture probes (GS-1, METER Group, Inc., USA) buried at a depth of 2.5 cm to account for heat storage above the plates.

Post-processing of the flux data involved several standard corrections. These included a two-dimensional coordinate rotation to align the data, spectral adjustments following Moncrieff et al. (1997), and corrections for heat and water vapor density fluctuations based on the Webb et al. (1980) method. These corrections were implemented using Eddy Pro 7.0.6 software (Li-Cor, USA). Footprint analysis and data quality assessments were also performed using TOVI software (Li-Cor, USA). Detailed insights into the specifics of the flux tower and energy closure for this site can be found in Peddinti and Kisekka (2022a), while the flux data processing methods are further elaborated in Bambach et al. (2022). The flux tower footprint model was developed using the framework proposed by Kljun et al. (2002). The dataset for the CAPEX site spans from September 2020 to August 2022, encompassing 66 satellite images and multiple crop growth seasons.

For the three AmeriFlux towers, half-hourly data was preprocessed and filtered based on quality assurance (QA) flags before being aggregated into daily ET estimates corresponding to Landsat overpasses. To address potential random and systematic errors in the EC measurements, two energy balance closure methods were considered: the Bowen ratio method and the residual latent heat flux method (Mauder et al., 2013). The focus was not on the specific closure method used but rather on ensuring that the EC measurements adhered to the principle of energy conservation. In this study, the residual latent heat flux method was applied to correct the measured data, ensuring that the observed energy fluxes, particularly latent heat, were consistent with the conservation of energy.

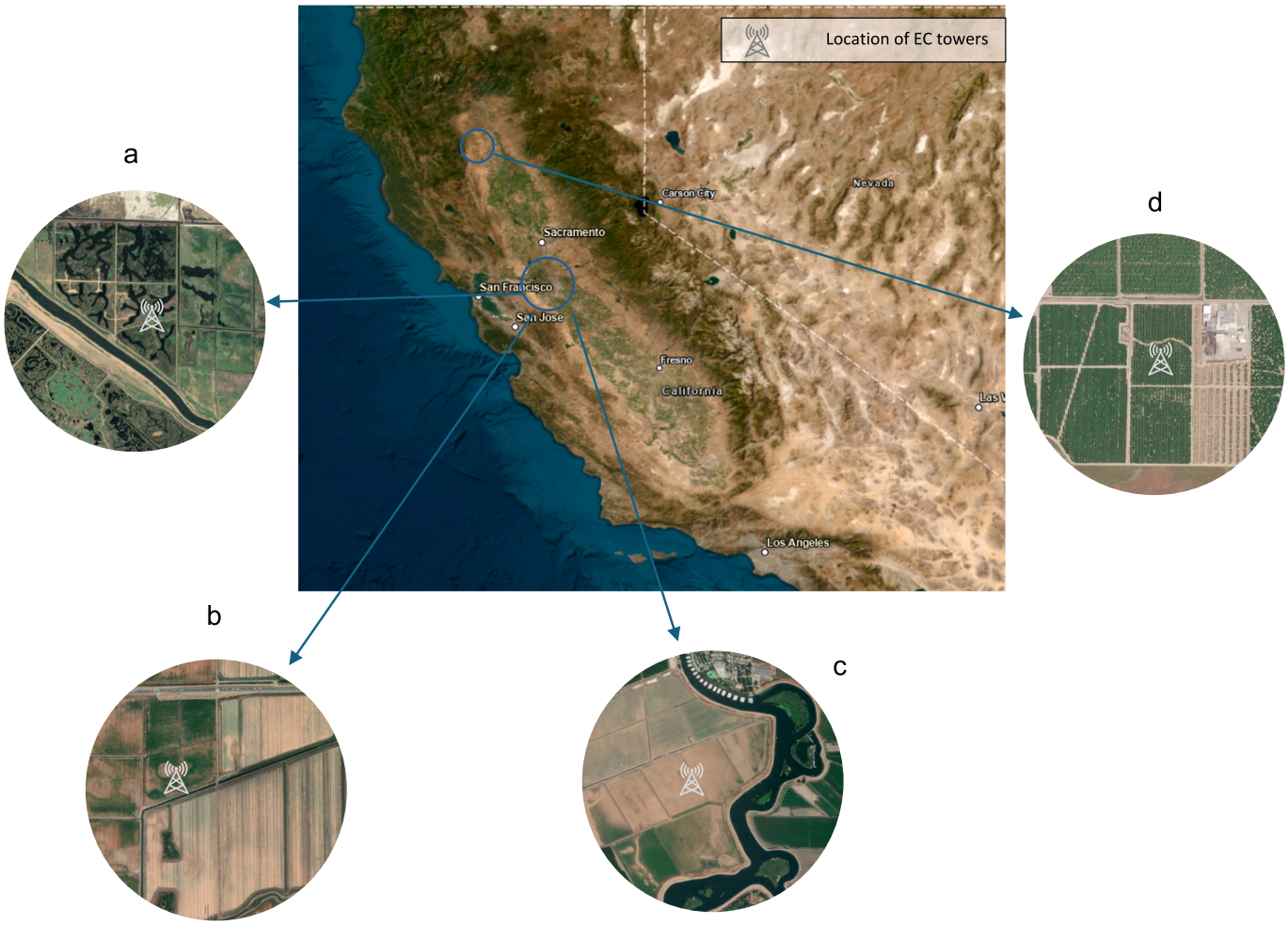

Fig. 2. Study site locations a) US-Myb, b) US-Bi2, c) US-Bi1, d) a commercial almond orchard at the CAPEX ranch located near Corning California in the Sacramento Valley.

2.3. Methodological framework

The proposed framework, illustrated in Fig. 2, consists of five key components: (I) Input data collection, including meteorological, remote sensing, and eddy covariance (EC) data; (II) SEBAL model configuration; (III) Sensitivity analysis (SA); (IV) Model calibration and Bayesian inference using the DREAM algorithm; and (V) Validation of simulated ET against EC data. Sensitivity analysis is critical in identifying key parameters that significantly improve model optimization. In this study, SA was performed on meteorological inputs, a vital component of the SEBAL algorithm, and on the empirical equations used within the model. The DREAM algorithm is employed to derive posterior parameter distributions by integrating prior distributions (initial parameter estimates) with residual errors, represented by the likelihood function, which captures the discrepancies between model predictions and observed data.

2.4. Description of the SEBAL algorithm

The SEBAL methodology determines ET as a residual of the surface energy balance equation. In this study, this approach will hereafter be referred to as SEBAL-ORG. The net radiation (R_n) at the surface is partitioned into soil heat flux (G), sensible heat flux (H), and latent heat flux (λET) all expressed in units of W m^{-2}. The relationship is given by the Eq. (1):

$$\lambda ET = R_n - G - H \tag{1}$$

This equation indicates that the latent heat flux, which corresponds to ET, is the remaining energy after accounting for the soil heat flux and sensible heat flux. Essentially, the energy not used to heat the soil or air is used for ET.

Net radiation is the balance of incoming and outgoing long- and short-wave radiation:

$$R_n = (1-\alpha)R_{s\downarrow} + R_{L\downarrow} - R_{L\uparrow} - (1-\varepsilon_0)R_{L\downarrow} \tag{2}$$

where $R_{s\downarrow}$ is the incoming short-wave radiation, and $R_{L\downarrow}$ and $R_{L\uparrow}$ are incoming and outgoing longwave radiation, respectively. α is surface albedo (−) estimated according to Tasumi et al. (2008). ε_0 is the surface thermal emissivity determined from vegetative indices such as NDVI (Van De Griend and Owe, 1993).

The long-wave radiation incidents are computed by the Stefan-Boltzmann equation (Boltzmann, 1978) as follow:

$$R_{L\uparrow} = \sigma\varepsilon_0 T_s^4 \tag{3}$$

$$R_{L\downarrow} = \sigma\varepsilon_a T_a^4 \tag{4}$$

where T_s and T_a are surface temperature and air temperature (K), and σ is the Stefan-Boltzmann constant, 5.67 × 10–8 W m^{-2} K^{-4}. The emissivity of the atmosphere (ε_a) is estimated through an empirical equation suggested by Bastiaanssen et al. (1998a):

$$\varepsilon_a = \beta_1(-ln\tau_{sw})^{\beta_2} \tag{5}$$

where the term τ_{sw} is the broad-band atmospheric transmissivity (dimensionless), computed according to Allen et al. (1998). β_1 and β_2 are assumed 0.85 and 0.09 as suggested by Allen et al. (2007b); and Bastiaanssen et al. (1998b).

The second component of energy balance, soil heat flux (G), is estimated as follows:

$$G/R_n = (T_s - 273.15)(\beta_3 + \beta_4\alpha)\left(1 - 0.98NDVI^4\right) \tag{6}$$

β_3 and β_4 are empirical parameters with default values of 0.0038 and 0.0074, respectively.

H is the rate of heat loss to the air through convection and conduction driven by temperature differential at two specific heights. The estimation of H in SEBAL is done through an iterative process:

$$H = \frac{\rho C_P dT}{r_{ah}} \tag{7}$$

where ρ is the air density (kg m^{-3}), Cp is the specific heat of air at constant pressure (J/kg/K), r_{ah} is the aerodynamic resistance (s m^{-1}) for heat transfer, and dT is the temperature difference between two near-surface heights (z_2, z_1). dT is linearly related to surface temperature where two empirical coefficients (a and b) are determined for two extreme anchor pixels:

$$dT = a + bT_s \tag{8}$$

r_{ah} is computed under conditions of neutral stability as:

$$r_{ah} = \frac{ln(z_2/z_1)}{u^* k} \tag{9}$$

where u* is friction velocity (m s^{-1}) quantifying the turbulent velocity fluctuations in the air, and k is the von Karman's constant (0.41). In SEBAL, atmospheric stability corrections are applied iteratively using the Monin-Obukhov length to account for buoyancy effects under stable and unstable conditions. This process adjusts aerodynamic resistance to ensure reliable estimates of sensible heat flux (H) and evapotranspiration (ET).

In the first iteration, the friction velocity is estimated using the logarithmic wind law for neutral atmospheric conditions:

$$u^* = \frac{k\, u_{200}}{ln(200/z_{om})} \tag{10}$$

where z_{om} is the surface roughness length that controls the momentum transfer (m), and u_{200} is the wind speed at 200 m where the surface roughness exerts no effect.

z_{om} for each pixel is computed through the empirical equation suggested by Raupach (1994):

$$z_{om} = (1-d/h)e^{(ku^*/U_h)-\psi} \tag{11}$$

$$\psi = lnc_w - 1 + 1/c_w \tag{12}$$

$$u^*/U_h = \sqrt{0.003 + 0.3LAI/2} \tag{13}$$

$$1 - d/h = \frac{1 - e^{-\sqrt{c_d LAI}}}{\sqrt{c_d LAI}} \tag{14}$$

where d is zero-plane displacement (m), h is obstacle or canopy height (m), U_h is the mean wind velocity at height h, LAI is the leaf area index and ψ is the roughness-sublayer influence function. The constants c_w and c_d are assumed to be free variables, typically set at 2 and 5, respectively.

Finally, once the components of energy balance are estimated, 24-h ET (ET_{24}) can be estimated as follows:

$$ET_{24} = \xi\, EF_{inst}\, R_{n_{24}}/\lambda \tag{15}$$

$$\xi = 1 + \left(\beta_5\, EF_{inst}\, e^{(VPD)\beta_6} - 1\right) \tag{16}$$

EF_{inst} is the evaporative fraction calculated from the ratio of the instantaneous latent heat to the difference between Rn and G, $R_{n_{24}}$ daily net radiation (W m^{-2}), λ latent heat of vaporization ξ is advection factor due to extra energy brought in by advection (Jaafar and Ahmad, 2020; McNaughton, 1976; Wei et al., 2023) and VPD is vapor pressure deficit (kPa). β_5 and β_6 are constants set to 0.985 and 0.008 by default, respectively.

2.5. Description of the DREAM algorithm

The adoption of Bayesian formalism allows for the derivation of the

posterior distribution of model parameters by conditioning model behavior on observed system response. The Bayesian inference can be formally expressed as follows (Kavetski et al., 2006; Vrugt, 2016):

$$p(\theta\ Y_{obs}) = \frac{p(\theta).p(Y_{obs}\theta)}{p(Y_{obs})} \propto p(\theta).L\ (\theta\ Y_{obs}) \tag{17}$$

where $p(\theta)$ and $p(\theta\ Y_{obs})$ signify the prior and posterior probability distribution, respectively. $L\ (\theta|Y_{obs})$ denotes the likelihood function determining the distance between the model behavior and the corresponding observed response. Marginal likelihood or evidence, $p(Y_{obs})$ acts as a normalization factor which is not required for posterior estimation. Assuming the error residuals are independent and normally distributed $e_t\ (\theta) \sim \mathcal{N}\left(0, \sigma_t^2\right)$ the likelihood function becomes:

$$L\ (\theta\ Y_{obs}, \sigma^2) = \prod_{t=1}^{n} \frac{1}{\sqrt{2\pi}\sigma}\ exp\left[\frac{1}{2}\left(\frac{y_t - y_{obs,t}}{\sigma_t}\right)^2\right] \tag{18}$$

where y_t and $y_{obs,t}$ denote simulated and observed system response (here, ET) at time step t, respectively and σ_t is the standard deviation of model error.

After defining the prior distribution and likelihood function, the next step is to sample the posterior distribution effectively. At this stage, the DREAM algorithm—a powerful multi-chain Markov Chain Monte Carlo (MCMC) sampler—is utilized to sample from the posterior distribution efficiently (Laloy and Vrugt, 2012; Vrugt, 2016). The DREAM algorithm operates by running multiple Markov chains concurrently. Each chain proposes candidate solutions that explore the parameter space, ultimately converging toward the posterior distribution—an updated belief about the parameters conditioned on the observed data and model.

The process, illustrated in Fig. 3, consists of several key steps:

1. Generate Candidates: The algorithm begins by generating candidate parameter vectors for each of the sensitive parameters identified in the SEBAL model (Fig. 2). This is achieved by adapting the differences between randomly selected parameter vectors from multiple chains. The candidate generation step incorporates a differential evolution process combined with a small perturbation (ϵ), allowing for efficient exploration of the parameter space while ensuring diversity among the chains.
2. Crossover: The candidate parameters are adjusted based on a crossover probability CR in this step. If a random number U is less than 1 − CR, the candidate parameters are retained; otherwise, they are swapped with the parameters of the current chain. This allows the algorithm to maintain variability while encouraging convergence to the posterior distribution.
3. Evaluate Posterior: For each candidate set of parameters, the posterior probability is evaluated using Bayes' theorem, where the likelihood function and prior distributions are combined to estimate the updated parameter probabilities given the observed data.
4. Acceptance Probability: The proposed candidate's acceptance is determined by comparing the posterior probability of the candidate parameters with the current parameter set. The algorithm uses an acceptance probability formula (Fig. 3) to ensure that candidates with higher posterior probabilities are favored while still allowing some level of exploration.
5. Posterior Distribution: Once a candidate is accepted, the Markov chain moves to this new candidate. As this iterative process

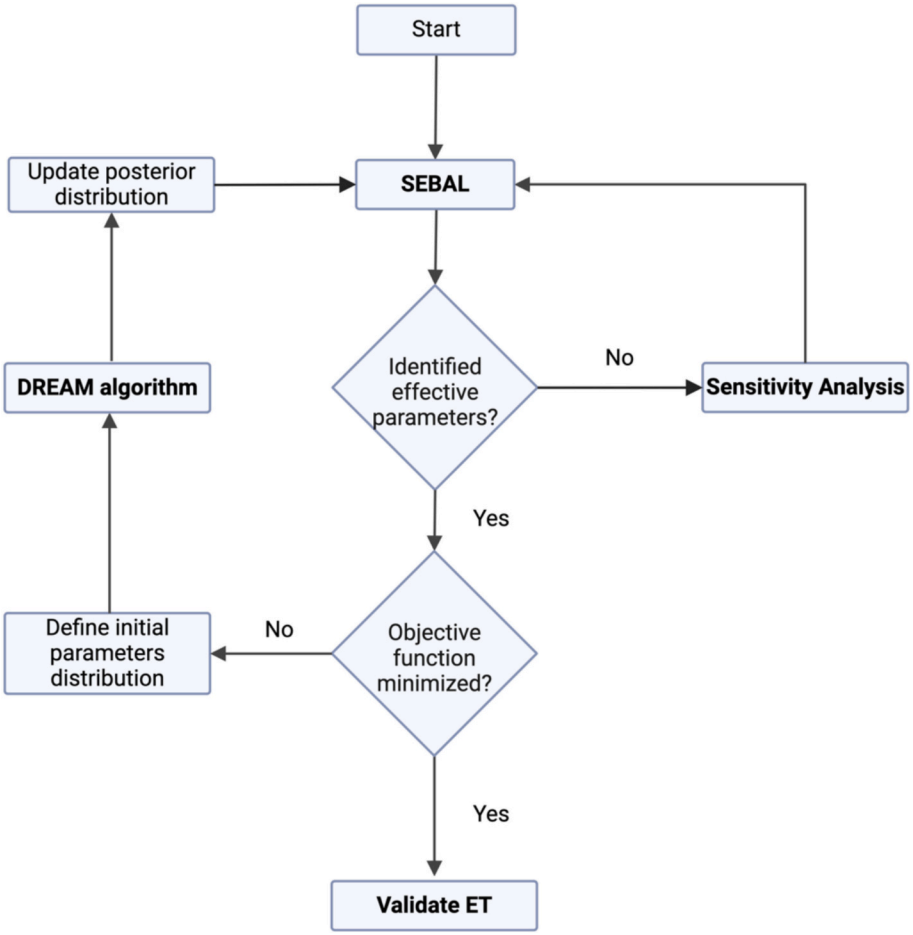

Fig. 3. Simplified workflow of the methodology including sensitivity analysis and optimization.

continues and the chains converge, the samples begin to represent the posterior distribution of the SEBAL model's parameters.

The DREAM algorithm's iterative nature, along with its adaptive multi-chain approach, allows it to effectively sample complex posterior distributions in high-dimensional parameter spaces. This results in more accurate estimates of the posterior distributions, which are critical for parameter uncertainty analysis and model calibration.

2.6. Introducing a new formulation for optimizing the SEBAL model

The selection of anchor pixels, specifically the hot and cold pixels within the image, typically relies on setting thresholds based on percentiles of NDVI and surface temperature. These thresholds help identify the extreme (hot and cold) end members from a candidate pool (Allen et al., 2013; Laipelt et al., 2021). Cold endmember candidates are chosen from well-vegetated areas, while hot endmember candidates are selected from the least vegetated fields. In our study, we introduced two equations into the optimization process, which we named thereafter SEBAL-OPT, to refine the selection of these extreme pixels after their initial identification:

$$H_{cold} = \text{selected } H_{cold} + \Omega_1(\text{selected } H_{hot} - \text{selected } H_{cold}) \quad (19)$$

$$H_{hot} = \text{selected } H_{hot} + \Omega_2\ (\text{selected } H_{hot} - \text{selected } H_{cold}) \quad (20)$$

where H_{cold} and H_{hot} are values of the cold and hot pixels after being modified, respectively, selected H_{cold} and H_{hot} are the endmember pixels selected out through NDVI and surface temperature filter, Ω_1 and Ω_2 are constants that are subject to optimization. This iterative refinement process helps optimize the hot and cold pixel selection to match the actual observations better.

We conducted a global sensitivity analysis using the FAST algorithm to support this refinement, focusing primarily on meteorological inputs and the constants in the SEBAL-ORG equations (Table 2). This analysis was essential for identifying the parameters that most significantly influence the performance of the SEBAL-OPT model. The key parameters considered for SA included: β1, β2, β3, β4, cd, cw, β5, β6, Ω1, and Ω2 (Table 2). Once the key parameters were identified through sensitivity analysis and incorporated into the calibration process. The objective of the calibration was to determine the optimal values of these parameters by minimizing the objective function and improving model performance in simulating ET.

SEBAL-OPT calibration was carried out using two approaches:

1. Temporal Calibration at the CAPEX Site: In this approach, calibration was performed using data from the first year (2020−2021) at the CAPEX almond orchard site. The optimized parameters were then validated against data from the second year (2022). The goal was to evaluate whether a single year of data could effectively calibrate the model for future years at the same location, potentially reducing the need for continuous year-over-year data collection.
2. Spatial Calibration across AmeriFlux Sites: In this approach, calibration was conducted using data from one AmeriFlux EC tower (US-Bi1). The optimized parameters were then validated using data from two other nearby EC towers (US-Bi2 and US-Myb), which represent different land use types—corn and wetland, respectively. This method assesses the model's accuracy when calibrated at one location but applied across sites with varying land use and environmental conditions, providing insights into the spatial generalizability of SEBAL-OPT.

The temporal calibration strategy at the CAPEX site assesses the model's ability to predict ET over time when calibrated using data from only one year. In contrast, the spatial calibration strategy across AmeriFlux sites evaluates the robustness of SEBAL-OPT when applied to different land use types and geographical conditions. Together, these approaches offer a comprehensive evaluation of SEBAL-OPT's adaptability across both temporal and spatial scales, aiming to achieve reliable ET estimations under varying climatic and agronomic conditions.

3. Results

3.1. Sensitivity analysis of SEBAL-ORG

Fig. 4 provides a visual representation of the sensitivity indices for each of the inputs and model parameters considered. Among all inputs, daily solar radiation emerged as the most sensitive, exerting a higher influence on the model outputs. This is expected, as solar radiation is the primary driver of the surface energy balance, and inaccuracies in its measurement can introduce considerable uncertainty into the ET estimates. This finding aligns with existing studies (e.g., Laipelt et al. (2021)) that similarly highlight the critical role of solar radiation in energy balance models. In contrast, other meteorological variables such as daily temperature, relative humidity, wind speed, and instantaneous solar radiation had minimal impact on the model outputs. This reduced sensitivity suggests that fluctuations in these inputs have a relatively minor influence on the overall accuracy of the SEBAL-ORG model.

When examining model parameters/constants, the selection of hot and cold pixels emerged as the most influential. This result aligns with the findings of Long et al. (2011), which emphasized the importance of anchor pixels in determining heat flux and, ultimately, ET. Among the two, the selection of hot pixels was notably more impactful than cold pixels in shaping the final ET estimates. This is because the hot pixels

Table 2
Parameters and their corresponding equations are considered in the global sensitivity analysis.

Functions	Parameters	Default value	Lower boundary	Higher boundary
$\varepsilon_a = \beta_1(-ln\tau_{sw})^{\beta_2}$	β_1	0.85	0.65	1.1
	β_2	0.09	0.08	0.3
$G/R_n = (T_s - 273.15)(\beta_3 + \beta_4\alpha)(1 - 0.98NDVI^4)$	β_3	0.0038	0.001	0.0055
	β_4	0.0074	0.003	0.009
	c_d	5	1	30
$z_{om} = (1 - d/h)e^{(ku^*/U_h)-\psi}$	c_w	2.5	2	10
	β_5	0.985	0.7	1.3
$\xi = 1 + (\beta_5\ EF_{inst}\ e^{(VPD)\beta_6} - 1)$	β_6	0.08	0.05	0.2
$H_{cold} = \text{selected } H_{cold} + \Omega_1(\text{selected } H_{hot} - \text{selected } H_{cold})$	Ω_1	0	−3	3
$H_{hot} = \text{selected } H_{hot} + \Omega_2\ (\text{selected } H_{hot} - \text{selected } H_{cold})$	Ω_2	0	−3	3

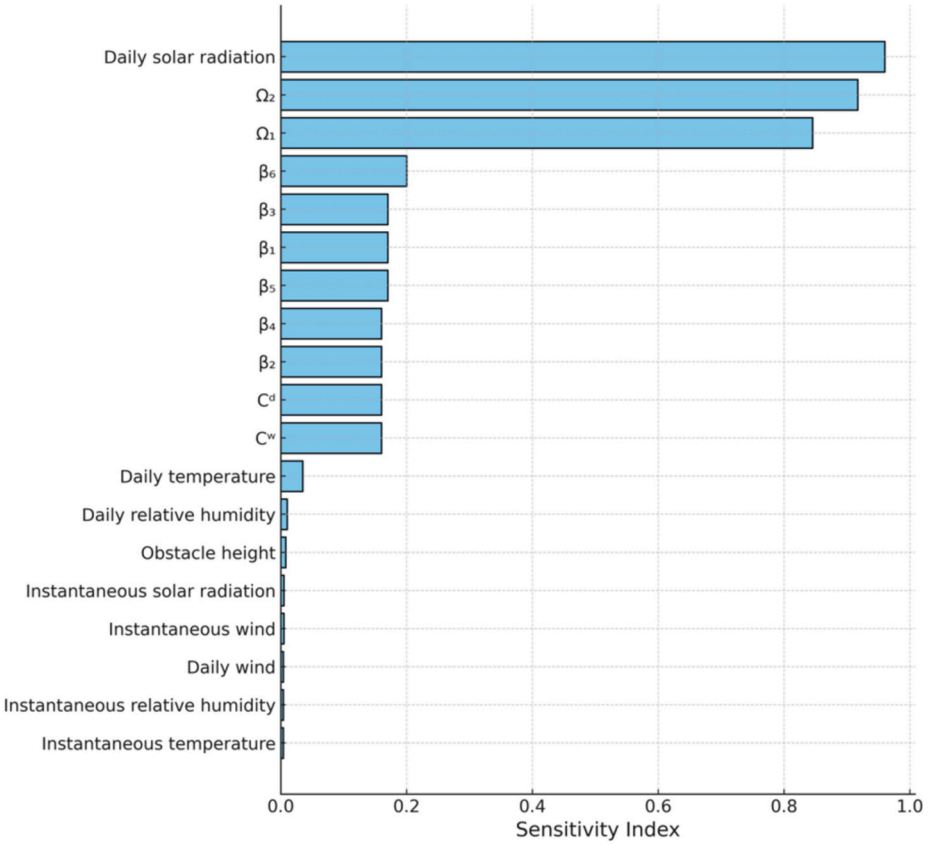

Fig. 4. Global sensitivity analysis of the SEBAL model using FAST algorithms.

represent the upper bound of surface temperature and heat flux in the model, which directly affects the latent heat flux and, consequently, the ET calculations. Fig. 4 underscores the importance of improving the accuracy in hot and cold pixel selection as a primary step to reduce uncertainty in ET estimations.

The findings of this global sensitivity analysis validate the focus on optimizing hot and cold pixel selection. Therefore, only these two parameters were considered for the calibration.

3.2. Optimization and accuracy assessment

The first row of Fig. 5 presents the results of the temporal calibration at the CAPEX site. The left panel shows the performance of SEBAL-ORG, while the right panel illustrates the improvements achieved with SEBAL-OPT. The temporal calibration approach resulted in marked improvements in ET estimation. SEBAL-OPT exhibited significantly reduced dispersion around the 1:1 line, with the R^2 increasing from 0.69 to 0.72 and the NSE improving from 0.15 to 0.69. The RMSE decreased from 1.39 mm d^{-1} with SEBAL-ORG to 0.84 mm d^{-1} with SEBAL-OPT, and the PBIAS shifted from a 29 % overestimation to a much-improved −7 %. These improvements suggest that SEBAL-OPT effectively reduces biases and enhances ET estimations' accuracy over time at the same site. Fig. 6 further demonstrates the benefits of temporal calibration at the CAPEX site. SEBAL-ORG consistently overestimated ET, particularly during peak growth periods, while SEBAL-OPT brought the ET estimates much closer to the observed EC measurements. This improvement is sustained over the entire validation year, highlighting the capability of SEBAL-OPT to produce reliable ET estimates beyond the initial calibration period. These results indicate that when applied to a single year of data, temporal calibration can effectively optimize the SEBAL model for use in subsequent years, making it a practical solution for long-term ET monitoring at the same site.

The second, third, and fourth rows of Fig. 5 display the results of the spatial calibration performed using data from the US-Bi1 tower and validated at the US-Bi2 and US-Myb towers. SEBAL-OPT consistently outperforms SEBAL-ORG across all three sites, demonstrating the effectiveness of the spatial calibration approach. At the US-Bi1 site, SEBAL-OPT improved the R^2 from 0.78 to 0.82 and the NSE from 0.59 to 0.80, with the RMSE decreasing from 1.03 mm d^{-1} to 0.72 mm d^{-1} and the PBIAS improving from −11.26 % to −4.04 %. These improvements indicate that the optimized parameters derived from SEBAL-OPT significantly enhanced the accuracy of ET predictions at the calibration site.

More importantly, the results from the validation sites (US-Bi2 and US-Myb) reveal that spatial calibration can effectively generalize the optimized parameters across diverse land use types. For example, at the US-Bi2 site, SEBAL-ORG had a considerable overestimation of ET, with an RMSE of 2.14 mm d^{-1} and a PBIAS of 41.25 %. After applying the parameters optimized through SEBAL-OPT at US-Bi1, the RMSE dropped to 1.33 mm d^{-1}, and the PBIAS improved to 22.78 %. Although this is still an overestimation, the improvement demonstrates that the model can reasonably generalize to other agricultural contexts. At the US-Myb site, classified as a permanent wetland, the SEBAL-ORG model showed poor performance, with an R^2 of 0.59 and an RMSE of 1.31 mm d^{-1}. However, SEBAL-OPT improved these values to an R^2 of 0.69 and an RMSE of 0.94 mm d^{-1}. The PBIAS improved from −19.69 % to 5.65 %, indicating a more balanced ET estimation in this unique environment. Fig. 6 shows the temporal comparison of simulated versus observed ET at the three sites. At US-Bi1, where the calibration occurred, SEBAL-OPT provides the best fit for the EC measurements. At US-Bi2 and US-Myb, SEBAL-OPT improved ET estimates significantly, even though the calibration was not directly applied at these sites. This demonstrates that spatial calibration can help SEBAL-OPT perform well across different land use types within the same geographic region without site-specific

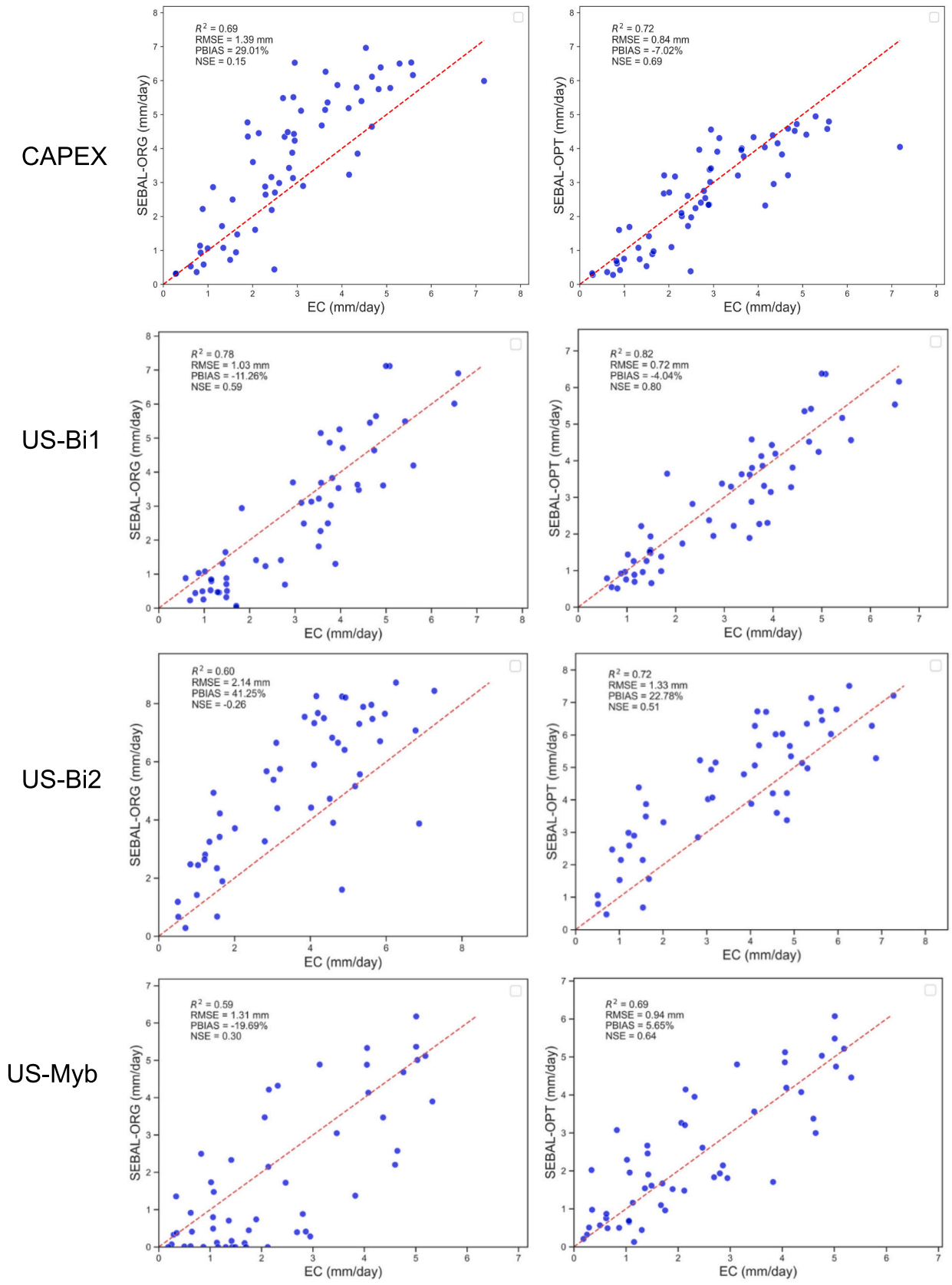

Fig. 5. Comparison of SEBAL model parameter optimization approaches; no optimization (SEBAL-ORG), optimized SEBAL (SEBAL-OPT) in 4 sites in California.

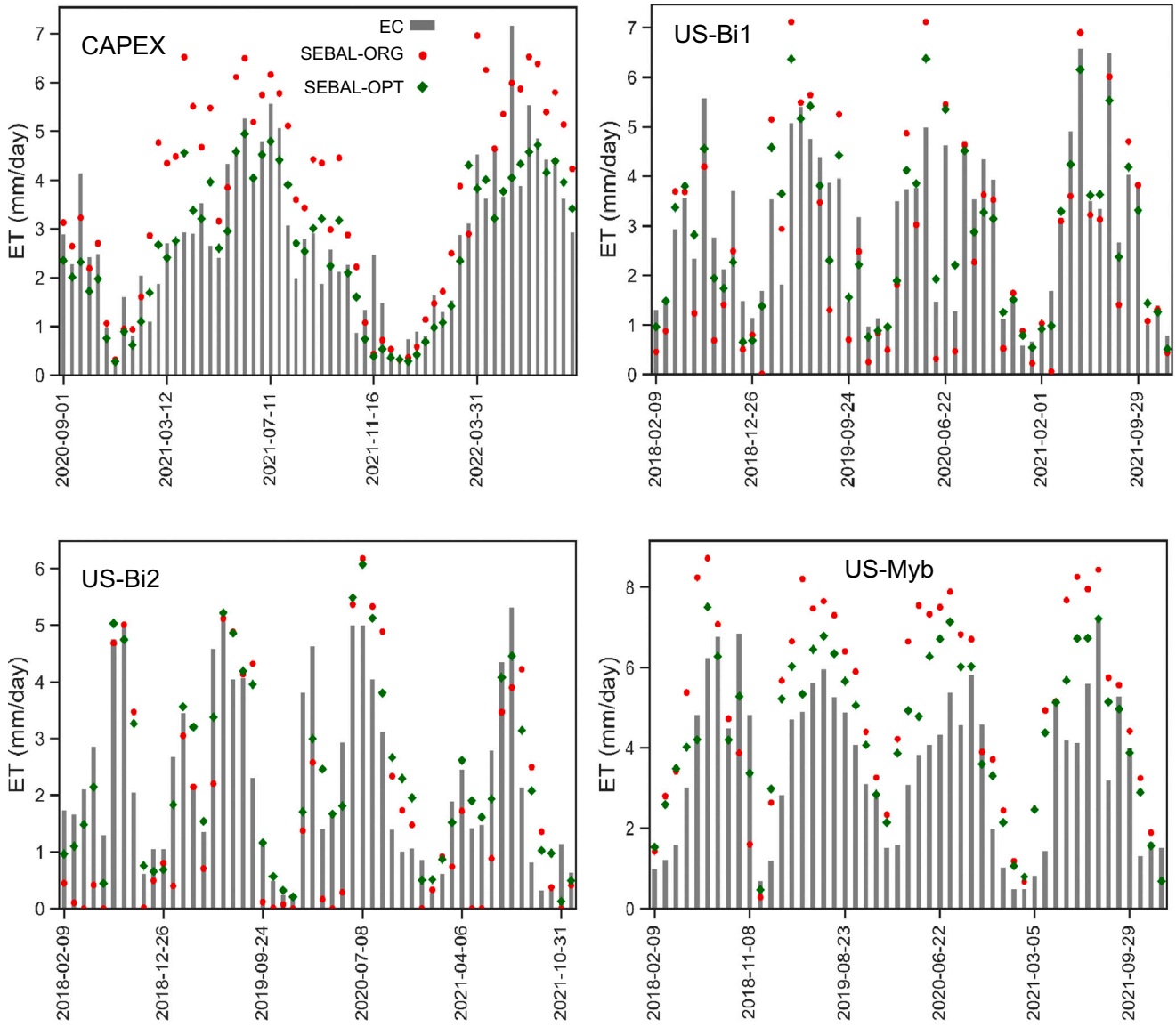

Fig. 6. Temporal variation of Evapotranspiration derived from SEBAL-ORG and SEBAL-OPT against Eddy Covariance ET.

recalibration.

As summarized in Table 3, both temporal calibration at the CAPEX site and spatial calibration across the AmeriFlux towers led to significant improvements in SEBAL-OPT's performance. The success of the temporal calibration demonstrates that SEBAL-OPT can provide reliable ET estimates for long-term monitoring at a single site after being calibrated with one year of data. Meanwhile, the spatial calibration approach confirms that SEBAL-OPT can generalize its optimized parameters to other land use types within the same region, ensuring accuracy in ET predictions even without site-specific recalibration. These results suggest that SEBAL-OPT has the potential to be a highly flexible and accurate model for ET estimation across diverse environments, opening the door to broader applications in regions where ground-based measurements are limited or unavailable.

3.3. Posterior distribution of hot and cold pixels

The DREAM algorithm was initiated with 5000 iterations to optimize the constants for hot and cold pixels (Ω_1 and Ω_2). The prior distributions were assumed to be uniform, with the initial ranges defined in Table 2.

Table 3
Summary statistics of SEBAL-ORG and SEBAL-OPT all sites. RMSE is in mm d^{-1}.

Site	SEBAL-ORG[1]				SEBAL-OPT[2]			
	r-squared	RMSE	PBIAS	NSE	r-squared	RMSE	PBIAS	NSE
CAPEX	0.69	1.39	29 %	0.15	0.72	0.84	−7.02 %	0.69
US-Bi1	0.78	1.03	−11.26 %	0.59	0.82	0.72	−4.04 %	0.8
US-Bi2	0.6	2.14	41.25 %	−0.26	0.72	1.33	22.78 %	0.51
US-Myb	0.59	1.31	−19.69 %	0.3	0.69	0.94	5.65 %	0.64

[1] SEBAL original.
[2] SEBAL optimized.

Given their high sensitivity, only Ω_1 and Ω_2 were selected for optimization. Fig. 7 presents the posterior distributions of Ω_1 and Ω_2 for the almond orchard and the US-Bi1 (alfalfa) sites. The histograms reflect the distribution of values for both constants after optimization, centering around the true values determined during the process. For the almond site, the distribution of the cold pixel constant Ω_1 is skewed significantly toward negative values, with a peak near −2. This indicates that the cold pixel initially selected by SEBAL was warmer than expected for a cold pixel, prompting the algorithm to adjust and 'cool down' this pixel during optimization. This adjustment effectively brought the cold pixel temperature closer to its optimal value for accurate ET estimation.

Similarly, at the US-Bi1 site, the cold pixel constant Ω_1 shows a comparable skewness toward negative values, clustering around −0.5. This pattern suggests that the cold pixel initially selected by SEBAL also required 'cooling down,' though to a lesser extent than the almond site, which indicates that the initial cold pixel temperature was closer to the ideal value in this case. In contrast, the posterior distribution for the hot pixel constant Ω_2 for the almond site is centered around zero, implying that the original selection of the hot pixel was relatively accurate. There was little need for adjustment during the optimization process, as the initial hot pixel temperature was already appropriate for accurate ET estimation. Interestingly, the distribution for the hot pixel does not extend into positive values, reinforcing the conclusion that no significant increase in temperature was necessary. For the US-Bi1 site, however, the distribution of the hot pixel constant Ω_2 is slightly shifted to the right, centering around 0.5. This pattern indicates that the initially selected hot pixel was cooler than expected, and the optimization process compensated by selecting a positive constant to adjust the pixel's temperature upwards. The histogram reveals that this adjustment was necessary to bring the hot pixel temperature closer to the ideal range for accurate ET estimation.

Fig. 8 presents example maps of evapotranspiration (ET) before and after the calibration process. As shown, the calibration introduces significant changes to the spatial distribution and variability of ET values compared to SEBAL-ORG. Additionally, shifts in the ET histograms are noticeable, indicating that the calibration not only affects spatial variations but also alters the overall statistical distribution of ET values. These shifts suggest improved alignment with ground-based measurements and a more accurate representation of the heterogeneity in water use across different land types.

Overall, the posterior distributions emphasize the role of optimization in refining the hot and cold pixel temperatures. At the almond site, the cold pixel required a more significant adjustment, while the hot pixel was already close to its optimal value. Conversely, at the US-Bi1 site, the hot pixel needed a slight upward adjustment, while the cold pixel required only a modest downward correction. These findings highlight the importance of accurately selecting anchor pixels, as their initial temperatures can significantly influence the accuracy of ET estimates in SEBAL.

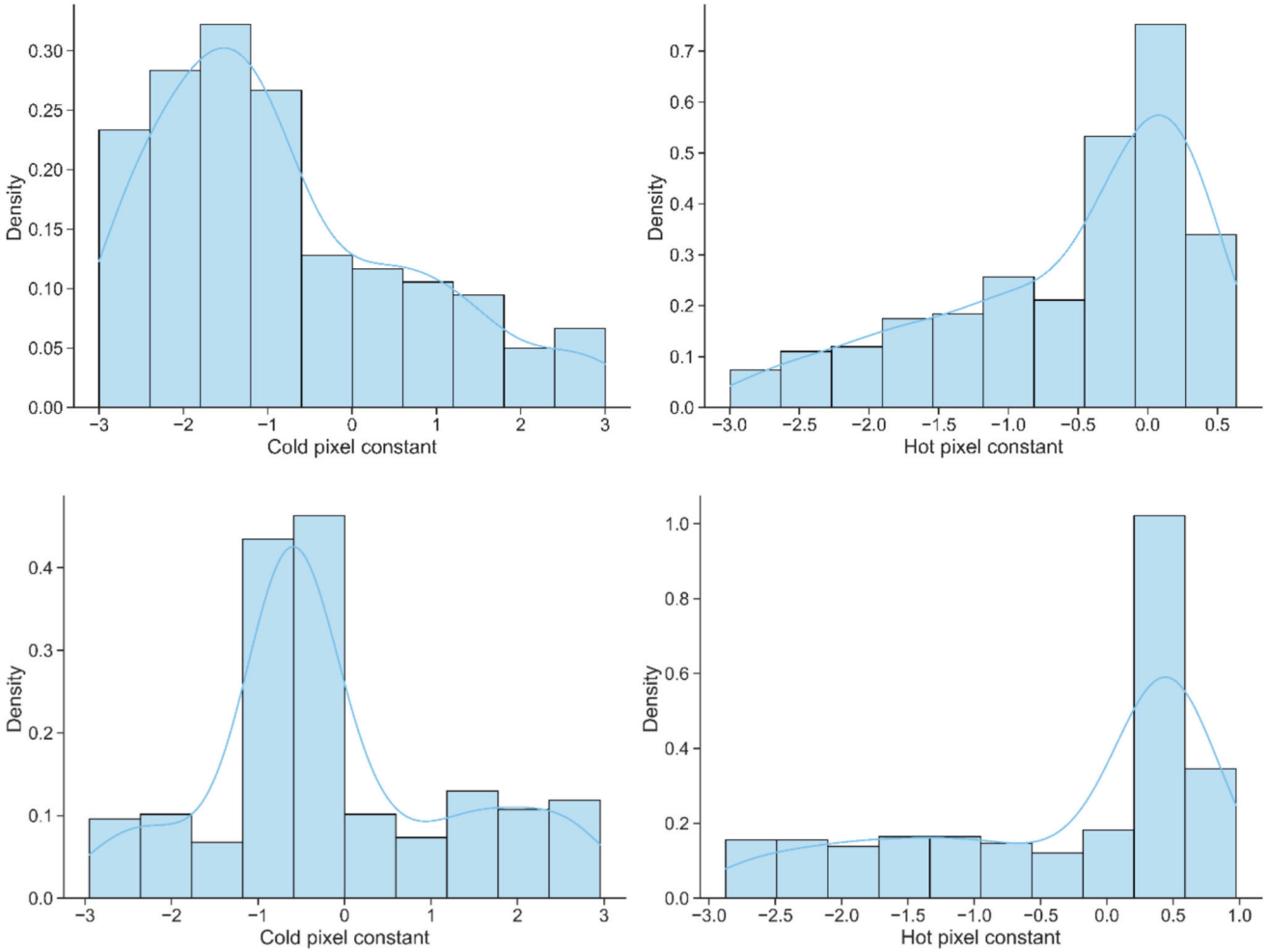

Fig. 7. Posterior probability density distribution for hot pixel constants and cold pixel constants for (a) almond orchard (CAPEX) (b) US-Bi1. Poster distributions as part of the output from the DiffeRential Evolution Adaptive Metropolis (DREAM).

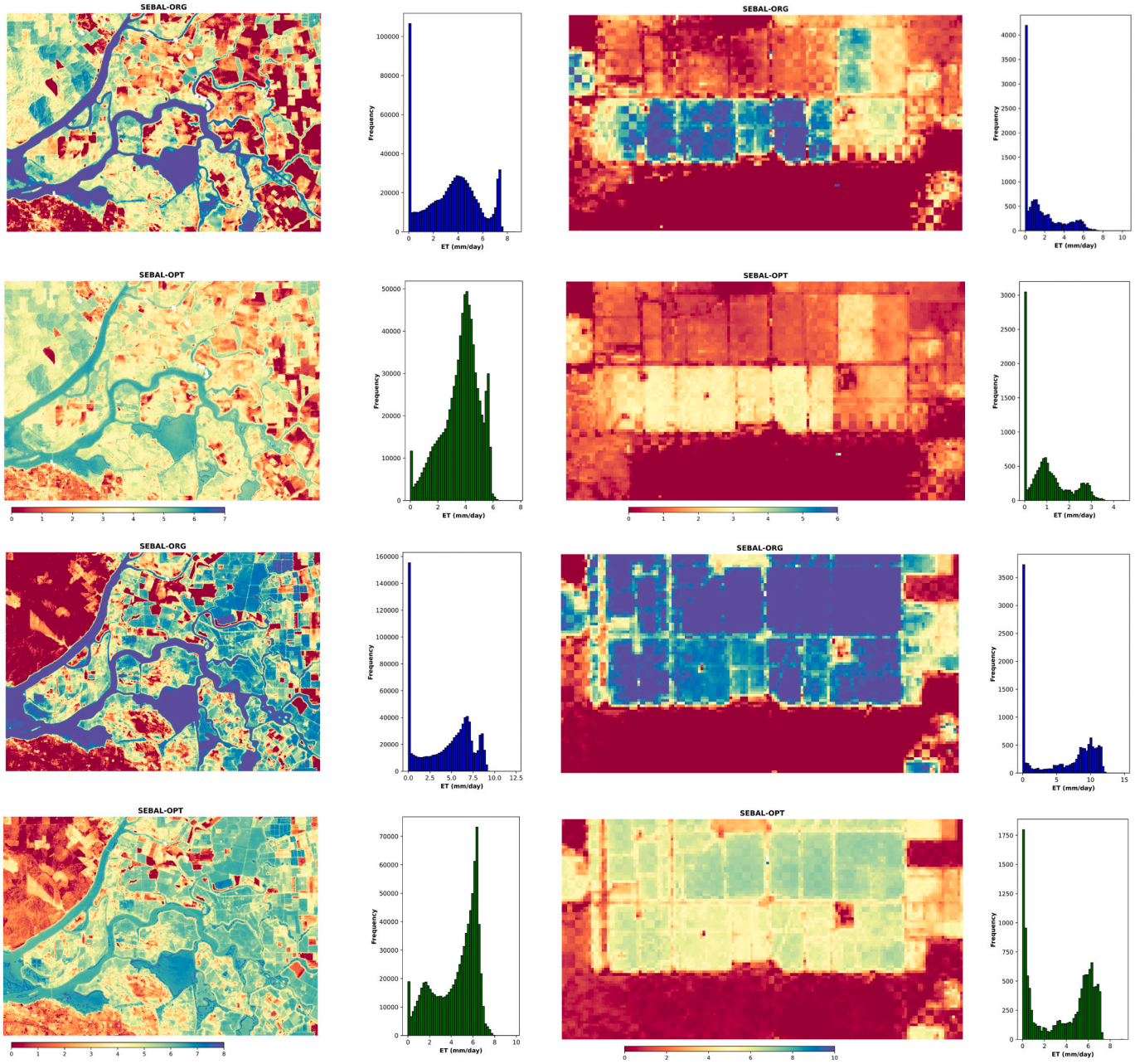

Fig. 8. Example daily ET maps of SEBAL original (SEBAL-ORG) versus SEBAL optimized (SEBAL-OPT). Figures are presented in pairs.

4. Discussion

ET is controlled by a combination of biological and environmental factors, with their influence varying across different land surface covers (Fang et al., 2016; Lei et al., 2018; Pan et al., 2020). Biological controls, such as vegetation type, leaf area index (LAI), stomatal conductance (Saugier and Katerji, 1991), and root depth, directly impact transpiration, a major component of ET (Yang et al., 2019). For instance, dense canopies with high LAI, such as forests, facilitate higher transpiration rates due to greater leaf surface area for water exchange, whereas sparse vegetation in semi-arid regions limits ET. Environmental factors such as sunlight, atmospheric temperature, wind dynamics, and soil water content (Du et al., 2021) determine the energy and moisture availability that drive evapotranspiration processes. In complex terrains, these controls are further modulated by topographic variability. The results of this study underscore the critical importance of precise parameter calibration in improving the accuracy of SEBAL model estimates. Specifically, the accurate identification of hot and cold pixels emerged as a key factor in reducing uncertainty in estimated ET values. Misidentification of these anchor pixels can lead to substantial errors in ET predictions, highlighting the need for careful calibration and parameter selection to enhance the reliability of SEBAL-based models. The sensitivity analysis demonstrated that, while SEBAL-based ET estimates are relatively insensitive to variations in meteorological inputs such as temperature, wind speed, and relative humidity, solar radiation remains a highly sensitive input. Therefore, while state-of-the-art global reanalysis datasets like ERA5 (Hersbach et al., 2020), CFSR (Saha et al., 2010), and GLDAS (Rodell et al., 2004) can be confidently used for SEBAL-based ET modeling over large scales or in data-scarce areas (Melton et al., 2022; Senay et al., 2022). Special attention must be paid to the accuracy of solar radiation data. Integrating solar radiation measurements from geostationary satellites (e.g. Diak et al., 2000) may improve ET estimates and reduce uncertainty.

The optimization results from the posterior distributions of the hot

and cold pixel constants further reinforce the importance of anchor pixel accuracy. At both the almond and US-Bi1 sites, adjustments to the cold pixel constants corrected initial discrepancies, resulting in more accurate ET predictions. This calibration process highlights that accurate pixel selection, informed by ground-based measurements such as EC data, can substantially enhance SEBAL's performance. The SEBAL-OPT model, which integrates both temporal and spatial calibration approaches, consistently outperformed the original SEBAL model (SEBAL-ORG), demonstrating the benefits of this optimized methodology across different land use types and geographical conditions.

Despite these advancements, a significant gap remains in the global sensitivity and uncertainty analysis of ET models (Cawse-Nicholson et al., 2020). As emphasized by Tran et al. (2023), robust sensitivity analysis and uncertainty propagation are essential for evaluating the performance of ET models. Their review showed that RMSE in ET models ranges from 0.01 to 6.65 mm d^{-1}, with an average of 1.12 mm d^{-1} across 2407 records. The RMSE values calculated in this study align with this range, confirming the validity of our findings. However, as temporal scales increase (e.g., from daily to weekly or monthly), RMSE typically decreases due to the smoothing effect of temporal aggregation.

It is important to note that validation results from one site may not be directly transferable to other locations, as controlling factors and uncertainties vary across different regions (K. Zhang et al., 2016). Therefore, validation metrics should be assessed individually for each site to ensure accurate interpretations of ET estimates. Future research should continue to focus on site-specific validation to understand better the variations in ET model performance across diverse environments. The optimization framework employed in this study has the potential to be applied to other energy balance-based ET models, such as DisALEXI, SEBS, METRIC, and SSEBop, and can be extended to a broader range of land cover types.

Although cross-model comparison was not the goal of this study, our analysis showed that SEBAL-OPT can outperform models such as DisALEXI, METRIC, and SSEBop at the four selected sites. The comparison, detailed in the supplementary material (Supplementary Material S1), shows that SEBAL-OPT exhibits reduced dispersion compared to the OpenET-based models. Additionally, statistical indicators confirm that SEBAL-OPT achieves higher accuracy through the integration of ground measurements (See Figs. S1 and S2). However, the availability and reliability of ground-based measurements, particularly from eddy covariance systems, remain critical for the successful implementation of these models. As demonstrated by SEBAL-OPT, incorporating high-quality, ground-based data significantly improves model accuracy, but challenges in data availability must be addressed to expand the applicability of these optimized models to other regions and land types. Advances in low-cost eddy covariance sensors, such as the Licor 710 sensors, offer promise for increasing the density of ground-based measurements that could be used in optimization frameworks such as the one presented in this study.

5. Conclusions

This study introduced a novel approach aimed at improving the accuracy and reducing the uncertainty of remotely sensed evapotranspiration (ET) estimates. We implemented this approach using the SEBAL model, enhanced through the integration of Bayesian inference to merge ground-based eddy covariance (EC) measurements with satellite data. The framework involved a global sensitivity analysis in identifying the most influential model parameters, which were then optimized using the DiffeRential Evolution Adaptive Metropolis (DREAM) algorithm.

Applying the SEBAL-OPT model across different land types resulted in significant improvements in ET estimation accuracy, particularly when compared to the original SEBAL algorithm. Validation results from four diverse sites highlighted SEBAL-OPT's enhanced performance, emphasizing the critical role of incorporating ground-based EC measurements in refining remote sensing models. The model's adaptability to various land types—from almond orchards to maize demonstrates its potential for broader application across different agroecosystems, a crucial consideration for large-scale water resource management.

The integration of ground-based EC data proved pivotal in these improvements, allowing the model to account for local variability that satellite data alone might not capture. This combination of satellite and ground-based data strengthens the reliability of ET estimates, which is particularly important for effective water allocation and resource management.

However, despite these advancements, certain limitations persist. The model's reliance on high-quality ground data poses a challenge in regions where such data are sparse or unreliable. Future research should investigate alternative data sources or explore other field measurement techniques, such as soil moisture data from sensors and lysimeters, to enhance the model's applicability in data-limited environments. Additionally, while this study focused on specific crop types and climates, further testing across a wider range of crops and climatic conditions is necessary to fully validate SEBAL-OPT's generalizability. Several other limitations should also be acknowledged. First, the energy balance closure issue inherent to eddy covariance (EC) measurements may introduce some uncertainty into the validation results. Second, the spatial scale mismatch between Landsat satellite imagery pixels and the EC flux tower footprint could affect direct comparisons, particularly in heterogeneous landscapes. Future studies could explore techniques such as footprint modeling or integrating higher-resolution imagery to minimize this scale discrepancy. Finally, cloud contamination in satellite imagery, especially under all-sky conditions, may limit the availability of cloud-free data for ET estimation. Incorporating alternative satellite data sources, such as Sentinel-2 or MODIS, or developing robust gap-filling techniques could help address this limitation and improve the model's performance in cloudy regions. These considerations highlight key avenues for further enhancing SEBAL-OPT's accuracy, robustness, and applicability across diverse environmental and agricultural conditions.

If adopted widely, this framework could significantly improve water allocation and demand monitoring, helping stakeholders such as policymakers, water managers, and farmers make better-informed decisions. By enhancing the accuracy of ET estimation, SEBAL-OPT can support optimized irrigation practices and contribute to the sustainable management of water resources across diverse agricultural landscapes.

CRediT authorship contribution statement

Ali Karbalaye Ghorbanpour: Writing – original draft, Visualization, Validation, Methodology, Investigation, Formal analysis, Conceptualization. **Srinivasa Rao Peddinti:** Writing – review & editing, Methodology, Formal analysis. **Tim Hessels:** Writing – review & editing, Methodology. **Wim Bastiaanssen:** Writing – review & editing, Methodology. **Isaya Kisekka:** Writing – review & editing, Validation, Supervision, Project administration, Methodology, Funding acquisition, Formal analysis, Conceptualization.

Declaration of competing interest

The authors declare that they have no known competing financial interests or personal relationships that could have appeared to influence the work reported in this paper.

Acknowledgments

This study was supported by the USDA NIFA Award # 2021-68012-35914, USDA NRCS CEAP Award # NR193A750023C016, and Almond Board of California Grant Project HORT69 Kisekka.

Appendix A. Supplementary data

Supplementary data to this article can be found online at https://doi.org/10.1016/j.scitotenv.2025.178530.

Data availability

Data will be made available on request.

References

Abbaspour, K.C., Yang, J., Maximov, I., Siber, R., Bogner, K., Mieleitner, J., Zobrist, J., Srinivasan, R., 2007. Modelling hydrology and water quality in the pre-alpine/alpine Thur watershed using SWAT. J. Hydrol. 333 (2–4), 413–430. https://doi.org/10.1016/J.JHYDROL.2006.09.014.

Abbaspour, K.C., Rouholahnejad, E., Vaghefi, S., Srinivasan, R., Yang, H., Kløve, B., 2015. A continental-scale hydrology and water quality model for Europe: calibration and uncertainty of a high-resolution large-scale SWAT model. J. Hydrol. 524, 733–752. https://doi.org/10.1016/J.JHYDROL.2015.03.027.

Allen, R.G., Pereira, L.S., Raes, D., Smith, M., 1998. Crop evapotranspiration-guidelines for computing crop water requirements-FAO irrigation and drainage paper 56. Fao, Rome, 300(9), p. D05109.

Allen, R.G., Tasumi, M., Trezza, R., 2007a. Satellite-based energy balance for mapping evapotranspiration with internalized calibration (METRIC)—model. J. Irrig. Drain. Eng. 133 (4), 380–394. https://doi.org/10.1061/(ASCE)0733-9437(2007)133:4(380).

Allen, R.G., Tasumi, M., Trezza, R., 2007b. Satellite-based energy balance for mapping evapotranspiration with internalized calibration (METRIC)—model. Journal of Irrigation and Drainage Engineering 133 (4), 380–394.

Allen, R.G., Burnett, B., Kramber, W., Huntington, J., Kjaersgaard, J., Kilic, A., Kelly, C., Trezza, R., 2013. Automated calibration of the METRIC-Landsat evapotranspiration process. JAWRA Journal of the American Water Resources Association 49 (3), 563–576. https://doi.org/10.1111/JAWR.12056.

Anderson, M.C., Kustas, W.P., Norman, J.M., Hain, C.R., Mecikalski, J.R., Schultz, L., González-Dugo, M.P., Cammalleri, C., D'Urso, G., Pimstein, A., Gao, F., 2011. Mapping daily evapotranspiration at field to continental scales using geostationary and polar orbiting satellite imagery. Hydrol. Earth Syst. Sci. 15 (1), 223–239. https://doi.org/10.5194/HESS-15-223-2011.

Baldocchi, D., Falge, E., Gu, L., Olson, R., Hollinger, D., Running, S., Anthoni, P., Bernhofer, C., Davis, K., Evans, R., 2001. FLUXNET: A new tool to study the temporal and spatial variability of ecosystem-scale carbon dioxide, water vapor, and energy flux densities. Bull. Am. Meteorol. Soc. 82 (11), 2415–2434.

Bastiaanssen, W.G.M., Steduto, P., 2017. The water productivity score (WPS) at global and regional level: methodology and first results from remote sensing measurements of wheat, rice and maize. Sci. Total Environ. 575, 595–611. https://doi.org/10.1016/J.SCITOTENV.2016.09.032.

Bambach, N., Kustas, W., Alfieri, J., Gao, F., Prueger, J., Hipps, L., McKee, L., Castro, S.J., Alsina, M.M., McElrone, A.J., 2022. Inter-annual variability of land surface fluxes across vineyards: the role of climate, phenology, and irrigation management. Irrig. Sci. 40 (4–5), 463–480. https://doi.org/10.1007/s00271-022-00784-0.

Bastiaanssen, W.G.M., Menenti, M., Feddes, R.A., Holtslag, A.A.M., 1998a. A remote sensing surface energy balance algorithm for land (SEBAL). 1. Formulation. Journal of Hydrology 212–213 (1–4), 198–212. https://doi.org/10.1016/S0022-1694(98)00253-4.

Bastiaanssen, W.G.M., Menenti, M., Feddes, R.A., Holtslag, A.A.M., 1998b. A remote sensing surface energy balance algorithm for land (SEBAL). 1. Formulation. Journal of Hydrology 212–213 (1–4), 198–212. https://doi.org/10.1016/S0022-1694(98)00253-4.

Beven, K., Freer, J., 2001. Equifinality, data assimilation, and uncertainty estimation in mechanistic modelling of complex environmental systems using the GLUE methodology. J. Hydrol. 249 (1–4), 11–29. https://doi.org/10.1016/S0022-1694(01)00421-8.

Bhattarai, N., Quackenbush, L.J., Im, J., Shaw, S.B., 2017. A new optimized algorithm for automating endmember pixel selection in the SEBAL and METRIC models. Remote Sens. Environ. 196, 178–192. https://doi.org/10.1016/J.RSE.2017.05.009.

Boltzmann, L., 1978. Ableitung des Stefanschen Gesetzes, 1) betreffend die Abhängigkeit der Wärmestrahlung von der Temperatur aus der elektromagnetischen Lichttheorie. Von Kirchhoff Bis Planck 152–156. https://doi.org/10.1007/978-3-663-13885-3_11.

Cawse-Nicholson, K., Braverman, A., Kang, E.L., Li, M., Johnson, M., Halverson, G., Anderson, M., Hain, C., Gunson, M., Hook, S., 2020. Sensitivity and uncertainty quantification for the ECOSTRESS evapotranspiration algorithm – DisALEXI. International Journal of Applied Earth Observation and Geoinformation 89, 102088. https://doi.org/10.1016/J.JAG.2020.102088.

Diak, G.R., Bland, W.L., Mecikalski, J.R., Anderson, M.C., 2000. Satellite-based estimates of longwave radiation for agricultural applications. Agric. For. Meteorol. 103 (4), 349–355. https://doi.org/10.1016/S0168-1923(00)00141-6.

Du, M., Zhang, J., Wang, Y., Liu, H., Wang, Z., Liu, C., Yang, Q., Hu, Y., Bao, Z., Liu, Y., Jin, J., Zhou, X., Wang, G., 2021. Evaluating the contribution of different environmental drivers to changes in evapotranspiration and soil moisture, a case study of the Wudaogou Experimental Station. J. Contam. Hydrol. 243, 103912. https://doi.org/10.1016/J.JCONHYD.2021.103912.

Fang, Y., Sun, G., Caldwell, P., Mcnulty, S.G., Noormets, A., Domec, J.C., King, J., Zhang, Z., Zhang, X., Lin, G., Zhou, G., Xiao, J., Chen, J., 2016. Monthly land cover-specific evapotranspiration models derived from global eddy flux measurements and remote sensing data. Ecohydrology 9 (2), 248–266. https://doi.org/10.1002/ECO.1629.

FAO, 2018. WaPOR Database Methodology: Level 1. Remote Sensing for Water Productivity Technical Report: Methodology Series. FAO, Rome, Italy.

Foley, J.A., Ramankutty, N., Brauman, K.A., Cassidy, E.S., Gerber, J.S., Johnston, M., Mueller, N.D., O'Connell, C., Ray, D.K., West, P.C., Balzer, C., Bennett, E.M., Carpenter, S.R., Hill, J., Monfreda, C., Polasky, S., Rockström, J., Sheehan, J., Siebert, S., Zaks, D.P.M., 2011. Solutions for a cultivated planet. Nature 478 (7369), 337–342. https://doi.org/10.1038/nature10452.

Gao, Y., Long, D., Li, Z.L., 2008. Estimation of daily actual evapotranspiration from remotely sensed data under complex terrain over the upper Chao river basin in North China, 29(11), pp. 3295–3315. https://doi.org/10.1080/01431160701469073.

Hersbach, H., Bell, B., Berrisford, P., Hirahara, S., Horányi, A., Muñoz-Sabater, J., Nicolas, J., Peubey, C., Radu, R., Schepers, D., Simmons, A., Soci, C., Abdalla, S., Abellan, X., Balsamo, G., Bechtold, P., Biavati, G., Bidlot, J., Bonavita, M., Thépaut, J.N., 2020. The ERA5 global reanalysis. Q. J. Roy. Meteorol. Soc. 146 (730), 1999–2049. https://doi.org/10.1002/QJ.3803.

Jaafar, H.H., Ahmad, F.A., 2020. Time series trends of Landsat-based ET using automated calibration in METRIC and SEBAL: the Bekaa Valley, Lebanon. Remote Sensing of Environment 238, 111034. https://doi.org/10.1016/J.RSE.2018.12.033.

Jensen, M.E., Allen, R.G., 2016. Evaporation, evapotranspiration, and irrigation water requirements: Task Committee on Revision of Manual 70. (Issue Ed. 2). American Society of Civil Engineers (ASCE).

Jensen, M. E., & Wright, J. L. (n.d.). 67 Irrigation-Oriented et Models for the Great Plains 1.

Karimzadeh, S., Hartman, S., Chiarelli, D.D., Rulli, M.C., D'Odorico, P., 2024. The tradeoff between water savings and salinization prevention in dryland irrigation. Adv. Water Resour. 183, 104604. https://doi.org/10.1016/J.ADVWATRES.2023.104604.

Kavetski, D., Kuczera, G., Franks, S.W., 2006. Bayesian analysis of input uncertainty in hydrological modeling: 1. Theory. Water Resources Research 42 (3), 3407. https://doi.org/10.1029/2005WR004368.

Kisekka, I., Migliaccio, K.W., Muñoz-Carpena, R., Khare, Y., 2013. Sensitivity Analysis and Parameter Estimation for an Approximate Analytical Model of Canal-Aquifer Interaction Applied in the C-111 Basin. Trans. ASABE 56 (3), 977–992.

Kljun, N., Rotach, M.W., Schmid, H.P., 2002. A three-dimensional backward Lagrangian footprint model for a wide range of boundary-layer stratifications. Bound.-Lay. Meteorol. 103 (2), 205–226. https://doi.org/10.1023/A:1014556300021/METRICS.

Kuczera, G., Parent, E., 1998. Monte Carlo assessment of parameter uncertainty in conceptual catchment models: the Metropolis algorithm. J. Hydrol. 211 (1–4), 69–85. https://doi.org/10.1016/S0022-1694(98)00198-X.

Kustas, W.P., Norman, J.M., 1999. Evaluation of soil and vegetation heat flux predictions using a simple two-source model with radiometric temperatures for partial canopy cover. Agric. For. Meteorol. 94 (1), 13–29. https://doi.org/10.1016/S0168-1923(99)00005-2.

Laipelt, L., Henrique Bloedow Kayser, R., Santos Fleischmann, A., Ruhoff, A., Bastiaanssen, W., Erickson, T.A., Melton, F., 2021. Long-term monitoring of evapotranspiration using the SEBAL algorithm and Google Earth Engine cloud computing. ISPRS J. Photogramm. Remote Sens. 178, 81–96. https://doi.org/10.1016/J.ISPRSJPRS.2021.05.018.

Laloy, E., Vrugt, J.A., 2012. High-dimensional posterior exploration of hydrologic models using multiple-try DREAM(ZS) and high-performance computing. Water Resour. Res. 48 (1), 1526. https://doi.org/10.1029/2011WR010608.

Lei, H., Gong, T., Zhang, Y., Yang, D., 2018. Biological factors dominate the interannual variability of evapotranspiration in an irrigated cropland in the North China Plain. Agric. For. Meteorol. 250–251, 262–276. https://doi.org/10.1016/J.AGRFORMET.2018.01.007.

Long, D., Singh, V.P., Li, Z.L., 2011. How sensitive is SEBAL to changes in input variables, domain size and satellite sensor? J. Geophys. Res. Atmos. 116 (D21), 21107. https://doi.org/10.1029/2011JD016542.

Marx, A., Kunstmann, H., Schüttemeyer, D., Moene, A.F., 2008. Uncertainty analysis for satellite derived sensible heat fluxes and scintillometer measurements over Savannah environment and comparison to mesoscale meteorological simulation results. Agric. For. Meteorol. 148 (4), 656–667. https://doi.org/10.1016/J.AGRFORMET.2007.11.009.

Mauder, M., Cuntz, M., Drüe, C., Graf, A., Rebmann, C., Schmid, H.P., Schmidt, M., Steinbrecher, R., 2013. A strategy for quality and uncertainty assessment of long-term eddy-covariance measurements. Agric. For. Meteorol. 169, 122–135. https://doi.org/10.1016/J.AGRFORMET.2012.09.006.

McNaughton, K.G., 1976. Evaporation and advection I: evaporation from extensive homogeneous surfaces. Q. J. Roy. Meteorol. Soc. 102 (431), 181–191. https://doi.org/10.1002/QJ.49710243115.

McRae, G.J., Tilden, J.W., Seinfeld, J.H., 1982. Global sensitivity analysis—a computational implementation of the Fourier Amplitude Sensitivity Test (FAST). Comput. Chem. Eng. 6 (1), 15–25. https://doi.org/10.1016/0098-1354(82)80003-3.

Melton, F.S., Huntington, J., Grimm, R., Herring, J., Hall, M., Rollison, D., Erickson, T., Allen, R., Anderson, M., Fisher, J.B., Kilic, A., Senay, G.B., Volk, J., Hain, C., Johnson, L., Ruhoff, A., Blankenau, P., Bromley, M., Carrara, W., Anderson, R.G., 2022. OpenET: filling a critical data gap in water Management for the Western United States. JAWRA Journal of the American Water Resources Association 58 (6), 971–994. https://doi.org/10.1111/1752-1688.12956.

Moncrieff, J.B., Massheder, J.M., De Bruin, H., Elbers, J., Friborg, T., Heusinkveld, B., Kabat, P., Scott, S., Soegaard, H., Verhoef, A., 1997. A system to measure surface fluxes of momentum, sensible heat, water vapour and carbon dioxide. J. Hydrol. 188–189 (1–4), 589–611. https://doi.org/10.1016/S0022-1694(96)03194-0.

Monteith, J.L., 1981. Evaporation and surface temperature. Q. J. Roy. Meteorol. Soc. 107 (451), 1–27.
Morris, M.D., 1991. Factorial sampling plans for preliminary computational experiments. Technometrics 33 (2), 161–174.
Nagler, P.L., Scott, R.L., Westenburg, C., Cleverly, J.R., Glenn, E.P., Huete, A.R., 2005. Evapotranspiration on western U.S. rivers estimated using the Enhanced Vegetation Index from MODIS and data from eddy covariance and Bowen ratio flux towers. Remote Sens. Environ. 97 (3), 337–351. https://doi.org/10.1016/J.RSE.2005.05.011.
Pan, S., Pan, N., Tian, H., Friedlingstein, P., Sitch, S., Shi, H., Arora, V.K., Haverd, V., Jain, A.K., Kato, E., Lienert, S., Lombardozzi, D., Nabel, J.E.M.S., Ottlé, C., Poulter, B., Zaehle, S., Running, S.W., 2020. Evaluation of global terrestrial evapotranspiration using state-of-the-art approaches in remote sensing, machine learning and land surface modeling. Hydrol. Earth Syst. Sci. 24 (3), 1485–1509. https://doi.org/10.5194/HESS-24-1485-2020.
Paul, G., Gowda, P.H., Vara Prasad, P.V., Howell, T.A., Staggenborg, S.A., Neale, C.M.U., 2013. Lysimetric evaluation of SEBAL using high resolution airborne imagery from BEAREX08. Adv. Water Resour. 59, 157–168. https://doi.org/10.1016/J.ADVWATRES.2013.06.003.
Peddinti, S.R., Kisekka, I., 2022a. Effect of aggregation and disaggregation of land surface temperature imagery on evapotranspiration estimation. Remote Sensing Applications: Society and Environment 27, 100805. https://doi.org/10.1016/J.RSASE.2022.100805.
Peddinti, S.R., Kisekka, I., 2022b. Effect of aggregation and disaggregation of land surface temperature imagery on evapotranspiration estimation. Remote Sensing Applications: Society and Environment 27, 100805. https://doi.org/10.1016/J.RSASE.2022.100805.
Penman, H.L., 1948. Natural evaporation from open water, bare soil and grass. Proceedings of the Royal Society of London. Series A. Mathematical and Physical Sciences 193 (1032), 120–145.
Raupach, M.R., 1994. Simplified expressions for vegetation roughness length and zero-plane displacement as functions of canopy height and area index. Bound.-Lay. Meteorol. 71 (1–2), 211–216. https://doi.org/10.1007/BF00709229/METRICS.
Remote sensing determination of evapotranspiration, 2023. Remote Sensing Determination of Evapotranspiration. https://doi.org/10.4060/CC8150EN.
Rodell, M., Houser, P.R., Jambor, U., Gottschalck, J., Mitchell, K., Meng, C.J., Arsenault, K., Cosgrove, B., Radakovich, J., Bosilovich, M., Entin, J.K., Walker, J.P., Lohmann, D., Toll, D., 2004. The global land data assimilation system. Bull. Am. Meteorol. Soc. 85 (3), 381–394. https://doi.org/10.1175/BAMS-85-3-381.
Saboori, M., Mokhtari, A., Afrasiabian, Y., Daccache, A., Alaghmand, S., Mousivand, Y., 2021. Automatically selecting hot and cold pixels for satellite actual evapotranspiration estimation under different topographic and climatic conditions. Agric Water Manag 248, 106763. https://doi.org/10.1016/J.AGWAT.2021.106763.
Saha, S., Moorthi, S., Pan, H.L., Wu, X., Wang, J., Nadiga, S., Tripp, P., Kistler, R., Woollen, J., Behringer, D., Liu, H., Stokes, D., Grumbine, R., Gayno, G., Wang, J., Hou, Y.T., Chuang, H.Y., Juang, H.M.H., Sela, J., Goldberg, M., 2010. The NCEP climate forecast system reanalysis. Bull. Am. Meteorol. Soc. 91 (8), 1015–1058. https://doi.org/10.1175/2010BAMS3001.1.
Saltelli, A., Bolado, R., 1998. An alternative way to compute Fourier amplitude sensitivity test (FAST). Computational Statistics & Data Analysis 26 (4), 445–460. https://doi.org/10.1016/S0167-9473(97)00043-1.
Saltelli, A., Aleksankina, K., Becker, W., Fennell, P., Ferretti, F., Holst, N., Li, S., Wu, Q., 2019. Why so many published sensitivity analyses are false: A systematic review of sensitivity analysis practices. Environ. Model. Software 114, 29–39. https://doi.org/10.1016/J.ENVSOFT.2019.01.012.
Saugier, B., Katerji, N., 1991. Some plant factors controlling evapotranspiration. Agric. For. Meteorol. 54, 263–277.
Senay, G.B., Friedrichs, M., Morton, C., Parrish, G.E.L., Schauer, M., Khand, K., Kagone, S., Boiko, O., Huntington, J., 2022. Mapping actual evapotranspiration using Landsat for the conterminous United States: Google earth engine implementation and assessment of the SSEBop model. Remote Sens. Environ. 275, 113011. https://doi.org/10.1016/J.RSE.2022.113011.
Shi, P., Yang, T., Yong, B., Xu, C.Y., Li, Z., Wang, X., Qin, Y., Zhou, X., 2023. Some statistical inferences of parameter in MCMC approach and the application in uncertainty analysis of hydrological simulation. J. Hydrol. 617, 128767. https://doi.org/10.1016/J.JHYDROL.2022.128767.
Silva, A.M., da Silva, R.M., Santos, C.A.G., 2019. Automated surface energy balance algorithm for land (ASEBAL) based on automating endmember pixel selection for evapotranspiration calculation in MODIS orbital images. Int. J. Appl. Earth Obs. Geoinf. 79, 1–11. https://doi.org/10.1016/J.JAG.2019.02.012.
Sobol, I.M., 2001. Global sensitivity indices for nonlinear mathematical models and their Monte Carlo estimates. Math. Comput. Simul. 55 (1–3), 271–280. https://doi.org/10.1016/S0378-4754(00)00270-6.
Song, X., Zhang, J., Zhan, C., Xuan, Y., Ye, M., Xu, C., 2015. Global sensitivity analysis in hydrological modeling: review of concepts, methods, theoretical framework, and applications. J. Hydrol. 523, 739–757. https://doi.org/10.1016/J.JHYDROL.2015.02.013.
Sriwongsitanon, N., Suwawong, T., Thianpopirug, S., Williams, J., Jia, L., Bastiaanssen, W., 2020. Validation of seven global remotely sensed ET products across Thailand using water balance measurements and land use classifications. Journal of Hydrology: Regional Studies 30, 100709. https://doi.org/10.1016/J.EJRH.2020.100709.
Su, Z., 2002. The Surface Energy Balance System (SEBS) for estimation of turbulent heat fluxes. Hydrol. Earth Syst. Sci. 6 (1), 85–100. https://doi.org/10.5194/HESS-6-85-2002.
Tasumi, M., Allen, R.G., Trezza, R., 2008. At-surface reflectance and albedo from satellite for operational calculation of land surface energy balance. J. Hydrol. Eng. 13 (2), 51–63. https://doi.org/10.1061/(ASCE)1084-0699(2008)13:2(51)/ASSET/48A30572-7261-4970-8891-919091474E0C/ASSETS/IMAGES/LARGE/7.JPG.
Teixeira, A.H. de C., Bastiaanssen, W.G.M., Ahmad, M.D., Bos, M.G., 2009. Reviewing SEBAL input parameters for assessing evapotranspiration and water productivity for the low-middle São Francisco River basin, Brazil: part A: calibration and validation. Agric. For. Meteorol. 149 (3–4), 462–476. https://doi.org/10.1016/J.AGRFORMET.2008.09.016.
Tran, B.N., van der Kwast, J., Seyoum, S., Uijlenhoet, R., Jewitt, G., Mul, M., 2023. Uncertainty assessment of satellite remote sensing-based evapotranspiration estimates: A systematic review of methods and gaps. EGUsphere 2023, 1–40.
Van De Griend, A.A., Owe, M., 1993. On the relationship between thermal emissivity and the normalized difference vegetation index for natural surfaces. Int. J. Remote Sens. 14 (6), 1119–1131. https://doi.org/10.1080/01431169308904400.
Volk, J.M., Huntington, J., Melton, F.S., Allen, R., Anderson, M.C., Fisher, J.B., Kilic, A., Senay, G., Halverson, G., Knipper, K., Minor, B., Pearson, C., Wang, T., Yang, Y., Evett, S., French, A.N., Jasoni, R., Kustas, W., 2023. Development of a benchmark Eddy flux evapotranspiration dataset for evaluation of satellite-driven evapotranspiration models over the CONUS. Agric. For. Meteorol. 331, 109307. https://doi.org/10.1016/J.AGRFORMET.2023.109307.
Vrugt, J.A., 2016. Markov chain Monte Carlo simulation using the DREAM software package: theory, concepts, and MATLAB implementation. Environ. Model. Software 75, 273–316. https://doi.org/10.1016/J.ENVSOFT.2015.08.013.
Vrugt, J.A., ter Braak, C.J.F., Gupta, H.V., Robinson, B.A., 2009. Equifinality of formal (DREAM) and informal (GLUE) Bayesian approaches in hydrologic modeling? Stoch. Env. Res. Risk A. 23 (7), 1011–1026. https://doi.org/10.1007/S00477-008-0274-Y/TABLES/3.
Wang, J., Sammis, T.W., Gutschick, V.P., Gebremichael, M., Miller, D.R., 2009. Sensitivity analysis of the surface energy balance algorithm for land (SEBAL). Trans. ASABE 52 (3), 801–811. https://doi.org/10.13031/2013.27401.
Webb, E.K., Pearman, G.I., Leuning, R., 1980. Correction of flux measurements for density effects due to heat and water vapour transfer. Q. J. Roy. Meteorol. Soc. 106 (447), 85–100. https://doi.org/10.1002/QJ.49710644707.
Wei, J., Cui, Y., Luo, Y., 2023. Rice growth period detection and paddy field evapotranspiration estimation based on an improved SEBAL model: considering the applicable conditions of the advection equation. Agric Water Manag 278, 108141. https://doi.org/10.1016/J.AGWAT.2023.108141.
Wolff, Wagner, Francisco, J.P., Flumignan, D.L., Marin, F.R., Folegatti, M.V., 2022. Optimized algorithm for evapotranspiration retrieval via remote sensing. Agric Water Manag 262, 107390. https://doi.org/10.1016/J.AGWAT.2021.107390.
Xie, H., Eheart, W., Chen, Y., Bailey, B.A., 2009. An approach for improving the sampling efficiency in the Bayesian calibration of computationally expensive simulation models. Water Resour. Res. 45 (6). https://doi.org/10.1029/2007WR006773.
Yang, Z., Zhang, Q., Hao, X., 2019. Environmental and biological controls on monthly and annual evapotranspiration in China's Loess Plateau. Theor. Appl. Climatol. 137 (3–4), 1675–1692. https://doi.org/10.1007/S00704-018-2701-4/TABLES/6.
Zhang, K., Kimball, J.S., Running, S.W., 2016. A review of remote sensing based actual evapotranspiration estimation. Wiley Interdiscip. Rev. Water 3 (6), 834–853. https://doi.org/10.1002/WAT2.1168.
Zhang, L., Yao, Y., Bei, X., Jia, K., Zhang, X., Xie, X., Jiang, B., Shang, K., Xu, J., Chen, X., 2019. Assessing the remotely sensed evaporative drought index for drought monitoring over Northeast China. Remote Sensing 11 (17), 1960. https://doi.org/10.3390/RS11171960.
Zhang, L., Marshall, M., Vrieling, A., Nelson, A., 2023. The divergence of energy- and water-balance evapotranspiration estimates in humid regions. J. Hydrol. 624, 129971. https://doi.org/10.1016/J.JHYDROL.2023.129971.